Influence of the geomagnetic field and of the uncertainties in the primary spectrum on the development of the muon flux in the atmosphere

P. Hansen, T. K. Gaisser, and T. Stanev
Bartol Research Institute, University of Delaware, Newark, Delaware 19716, USA

S. J. Sciutto
Departamento de Física and IFLP/CONICET, Universidad Nacional de La Plata, C. C. 67 - 1900 La Plata, Argentina
(Received 23 November 2004; published 21 April 2005)

In this paper we study the sensitivity of the flux of atmospheric muons to uncertainties in the primary cosmic ray spectrum and to the treatment of the geomagnetic field. We use the air shower simulation program AIRES to make the calculation for two different primary spectra and under several approximations to the propagation of charged particles in the geomagnetic field. The results illustrate the importance of accurate modeling of the geomagnetic field effects. We propose a high and a low fit of the proton and helium fluxes, and calculate the muon fluxes with these different inputs. Comparison with measurements of the muon flux by the CAPRICE experiment shows a slight preference for the higher primary cosmic ray flux parametrization.

DOI: 10.1103/PhysRevD.71.083012 PACS numbers: 96.40.De, 02.70.Rr, 96.40.Pq, 96.40.Tv

I. INTRODUCTION

The study of the muon fluxes in the atmosphere is currently of great interest because of the correlation between the muon and neutrino fluxes. Atmospheric neutrinos are produced from the decay channels of pions and kaons and the subsequent muon decay. The production of electron and muon neutrinos is dominated by the processes $\pi^+ \rightarrow \mu^+ + \nu_\mu$ followed by $\mu^+ \rightarrow e^+ + \overline{\nu}_\mu + \nu_e$ (and their charge conjugates), with a similar chain for charged kaons. When all particles decay, there will be two muon neutrinos for each electron neutrino resulting in an expected ratio of the flux of $\nu_\mu + \overline{\nu}_\mu$ to the flux of $\nu_e + \overline{\nu}_e$ of about 2. The experimental measurements [1–6] indicate, however, that the ratio of muon to electron neutrinos in the atmosphere is significantly smaller than 2.

This disagreement with theoretical predictions has been interpreted in terms of neutrino oscillations [7]. In order to calculate precisely the neutrino oscillation parameters one has to know the neutrino flux at production. Because of the close connection between the neutrinos and the muons, a standard test of codes used for calculating the neutrino flux is to calculate the muon flux with the same procedure and compare it to measurements of muons. Our approach here is related but somewhat different. We calculate only the muon flux, and we use the comparison with measurements to probe two aspects of the input that are common to both the neutrino and the muon fluxes.

The calculation of both muons and neutrinos starts with the primary spectrum outside the atmosphere. Therefore uncertainties in the measurements of the primary spectrum of protons, helium and heavier nuclei affect both fluxes in a similar way. Because the uncorrelated fluxes depend essentially on the all nucleon flux, heavy nuclei have relatively little effect, and the largest uncertainty in normalization comes from protons and helium. Experimental measurements of primary proton and helium spectra in

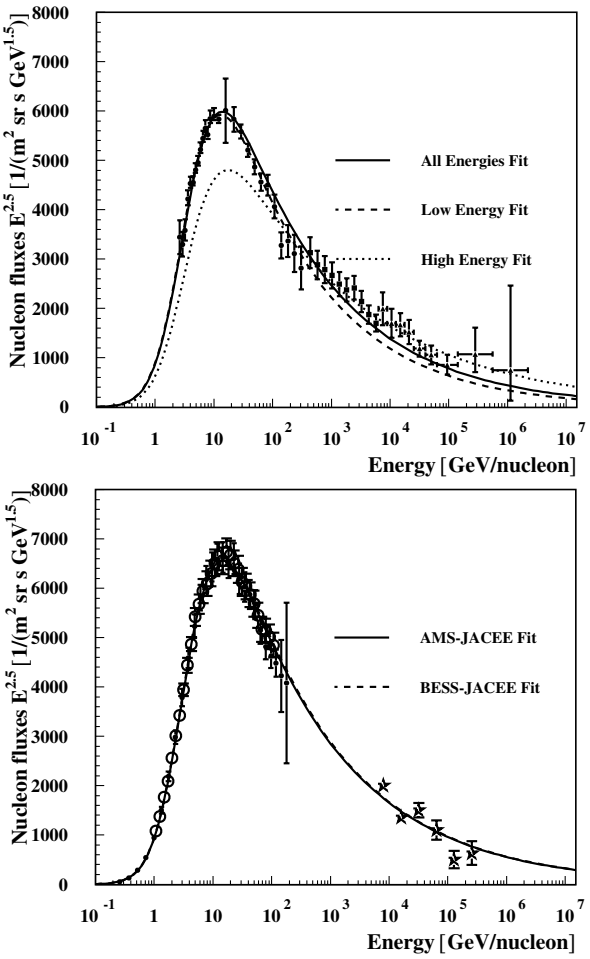

FIG. 1. Proton fluxes. The upper panel shows data from CAPRICE98 (full circle) Atic (black square) and RunJob (black triangle) (group 1) as function of the energy per nucleon. The lower panel shows data of AMS (full circle), BESS (open circle) and JACEE (star) (group 2) as function of the energy per nucleon.

some cases show significant differences from each other. We find that it is possible to divide the experimental data over a fairly large energy range into two groups: group 1 corresponds to the data which give a lower flux and group 2 to a higher flux. By making a ''high'' fit and a ''low'' fit over an extended energy range, we can define a reasonable range where the primary spectrum should lie. Comparison with measured muon fluxes may provide an extra constraint on the normalization of the primary flux.

Treatment of the geomagnetic field affects both the neutrino and the muon fluxes. One effect is a consequence of the field acting on the primary cosmic rays, which determines allowed and forbidden trajectories. Primaries on allowed trajectories reach the atmosphere to interact and produce secondary muons and neutrinos while those on forbidden trajectories do not reach the atmosphere and therefore do not contribute to the secondary fluxes. Which trajectories are allowed and which forbidden depends both on magnetic rigidity (defined as total momentum divided by charge of the nucleus) and on the direction of the

TABLE I. Parameters for the Hydrogen and Helium components in the fit of Eq. (1) for the two data groups.

Group	Component	α	k	b	c
1	Hydrogen	2.751 ± 0.004	14000 ± 130	2.15	0.21
1	Helium	2.734 ± 0.005	657 ± 8	1.25	0.14
2	Hydrogen	2.738 ± 0.004	15000 ± 160	2.15	0.21
2	Helium	2.639 ± 0.008	615 ± 16	1.25	0.14

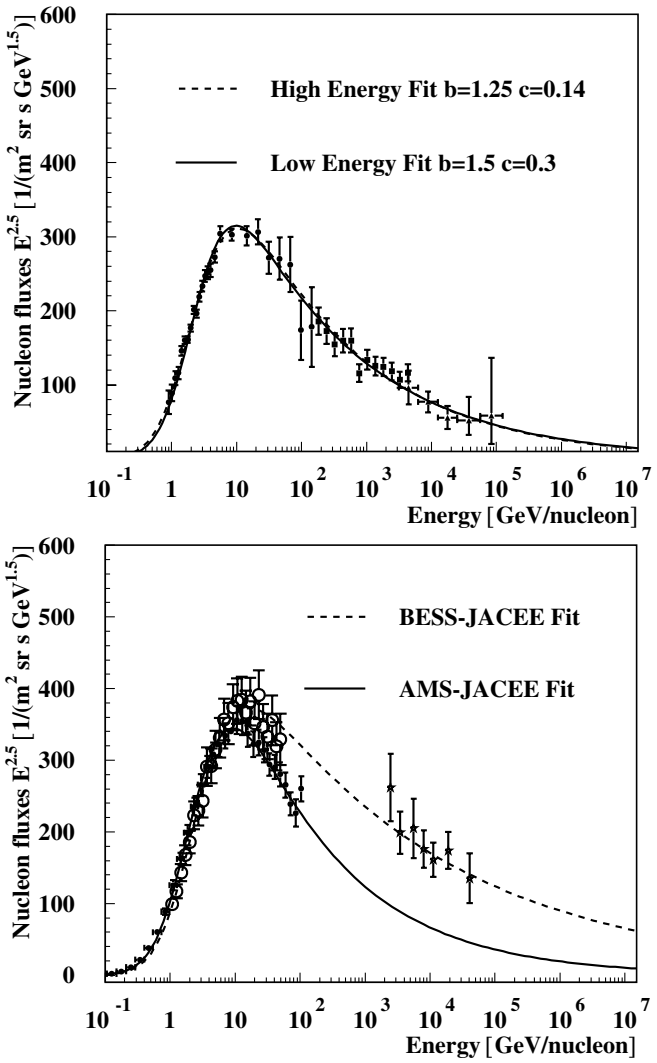

FIG. 2. Helium fluxes. The upper panel shows data from CAPRICE98 (full circle), Atic (black square) and RunJob (black triangle) (group 1) as function of the energy per nucleon. The lower panel shows data of AMS (full circle), BESS (open circle) and JACEE (star) (group 2) as function of the energy per nucleon.

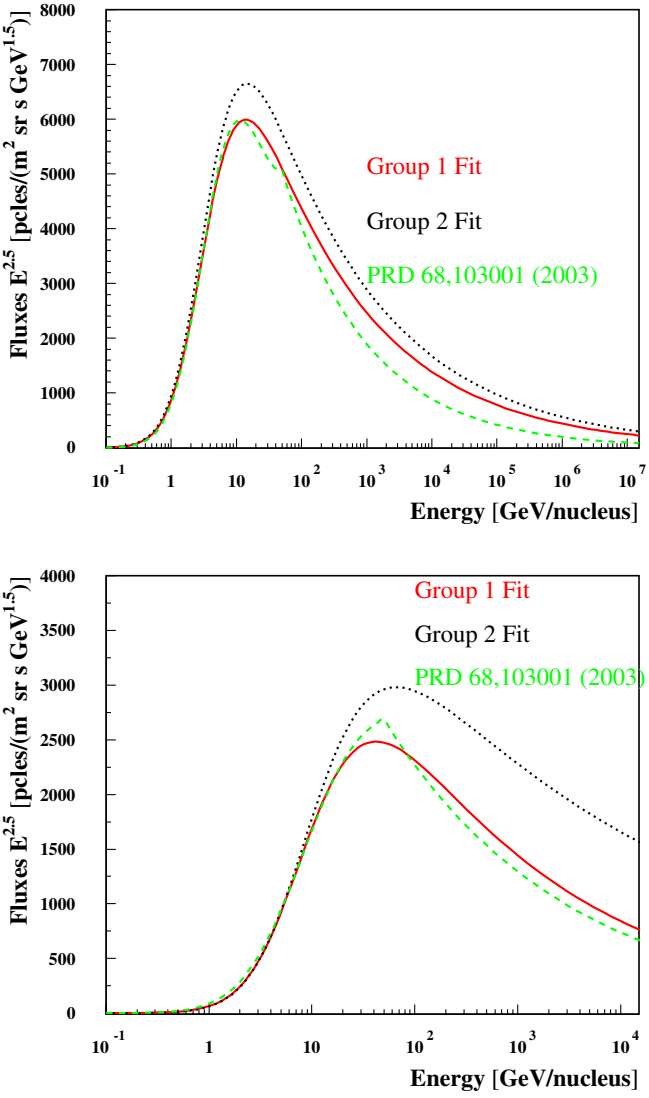

FIG. 3 (color online). Fits fluxes of proton (upper panel) and helium (lower panel) at the top of the atmosphere, plotted as function of the kinetic energy of the primaries. *(1)* Solid line: Group 1 fit. *(2)* Dotted line: Group 2 fit. *(3)* Dashed line: Input used in Ref. [15].

particle. At high geomagnetic latitudes all primaries with energies above pion production threshold are allowed. At low latitudes, particles need to have a minimum rigidity to reach the atmosphere, and this minimum value is higher for positive particles from the East than from the West. The other significant effect is the bending of charged muons after production in the atmosphere. We investigate the sensitivity of the muon fluxes to both aspects of the geomagnetic field as a function energy and atmospheric depth.

The paper is organized as follows: Sec. II is divided in three subsections. In II A we report on the method used to calculate the atmospheric muon fluxes; in II B we describe the treatment of the geomagnetic field; and in II C we propose the high and low fits of the primary proton and helium spectrum data. The results are reported in III and finally we summarize our conclusions in Sec. IV.

II. THE SIMULATIONS

A. Air shower simulations

In this work we have used the Air Shower Simulation Program (AIRES) [8,9], which provides full space-time particle propagation and accounts for the atmospheric density profile [10] and the Earth's curvature. The particles taken into account by AIRES in the simulation are: gammas, electrons, positrons, muons, pion, kaons, lambda baryons, nucleons, antinucleons and nuclei up to $Z = 36$. The hadronic processes are simulated using different event generators depending on the interaction energy.

High energy collisions are processed invoking an external package, SIBYLL or QGSJET (SIBYLL 2.1 [11] or QGSJET01 [12]), while low-energy ones are processed using an extension of the Hillas splitting algorithm (EHSA)[8,13,14]. EHSA implements the highly effective splitting algorithm suggested by A. M. Hillas with the addition of kaon production to the original model. In this work we use SIBYLL for high energy. The threshold energy separating the low and high energy regimes is 200 GeV.

Slightly more than half of atmospheric muons come from primary cosmic rays with energies in the range 10–100 GeV and less than 10% from primaries with energy greater than 1 TeV [15]. Therefore the choice of low-energy interaction model is very important for us. For a calculation of uncorrelated spectra of muons, production of charged pions by nucleons is by far the dominant process. Spectrum-weighted moments of the inclusive cross sections provide a useful way to compare different models. We have compared the extended Hillas splitting algorithm used here with several other hadronic event generators [16–18]. DPMjet [16], FLUKA [17], TARGET [18] and EHSA are essentially identical up to 30 GeV. Over the whole energy range from 10 to 200 GeV all four models lie within a range of 15%. Important for the result we find here is the fact that the representation of pion production that we use is on the high side of the range of models. We return to this point in the conclusion.

The effect of the geomagnetic field (GF) inside the atmosphere is taken into account in AIRES. The GF cal-

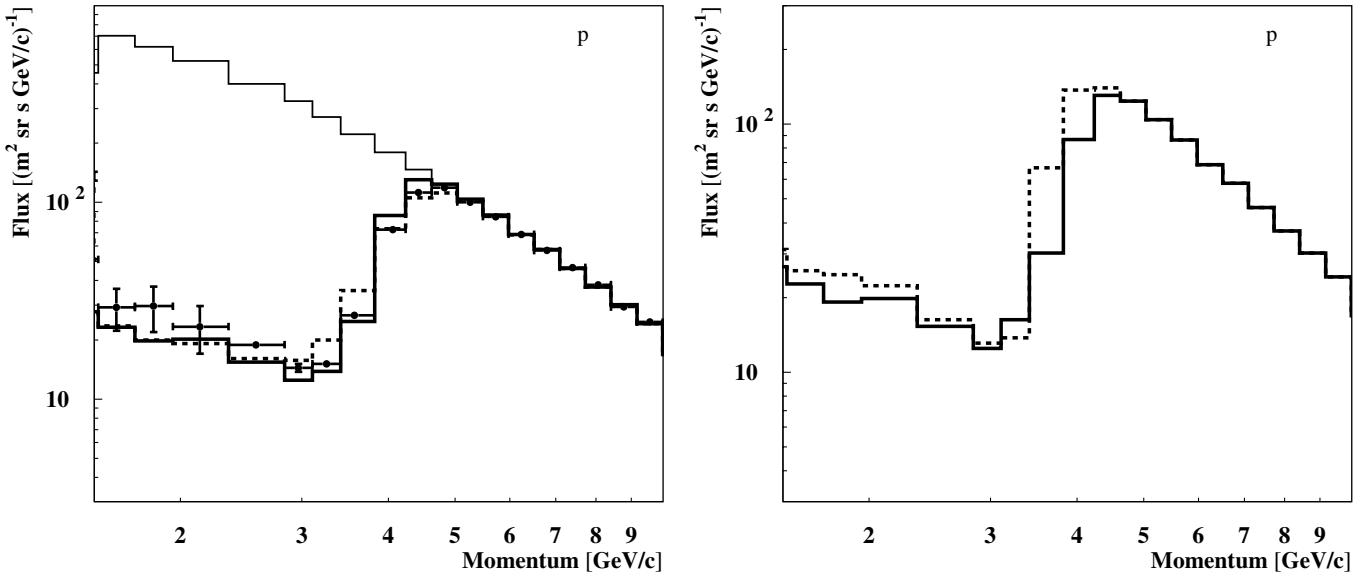

FIG. 4. Left: The solid points (•) represent the experimental proton flux measured by CAPRICE98 at Fort Summer for a residual atmospheric depth of 5.5 g/cm (PhD thesis E. Mocchiutti, Royal Institute of Technology). The lines are the simulated proton fluxes applying to the input spectrum: *(1)* a theoretical geomagnetic transmission function (dotted line). *(2)* The CAPRICE geomagnetic transmission function (wide solid line). *(3)* no geomagnetic transmission function (narrow solid line). Right: The lines are the simulated proton fluxes applying to the input spectrum: *(1)* Dotted line: a theoretical geomagnetic transmission function for particles coming from the West. *(2)* Wide solid line: a theoretical geomagnetic transmission function for cosmic rays that come from the East.

culations are controlled from the input instruction by specifying a date and the geographic coordinates of a site. The program uses the IGRF model [19] to evaluate the magnetic field intensity and orientation. It is assumed that the shower develops within a constant and homogeneous local magnetic field that is evaluated for the location of the detector before starting the simulations. The input used in the simulation and the procedure to calculate the flux is the same as that used in Ref. [15]. In Ref. [15] the CAPRICE experimental geomagnetic transmission function was used to estimate the cutoff prior to the calculation of the muon flux. Here we use a more precise backtracking method, as described in the next subsection.

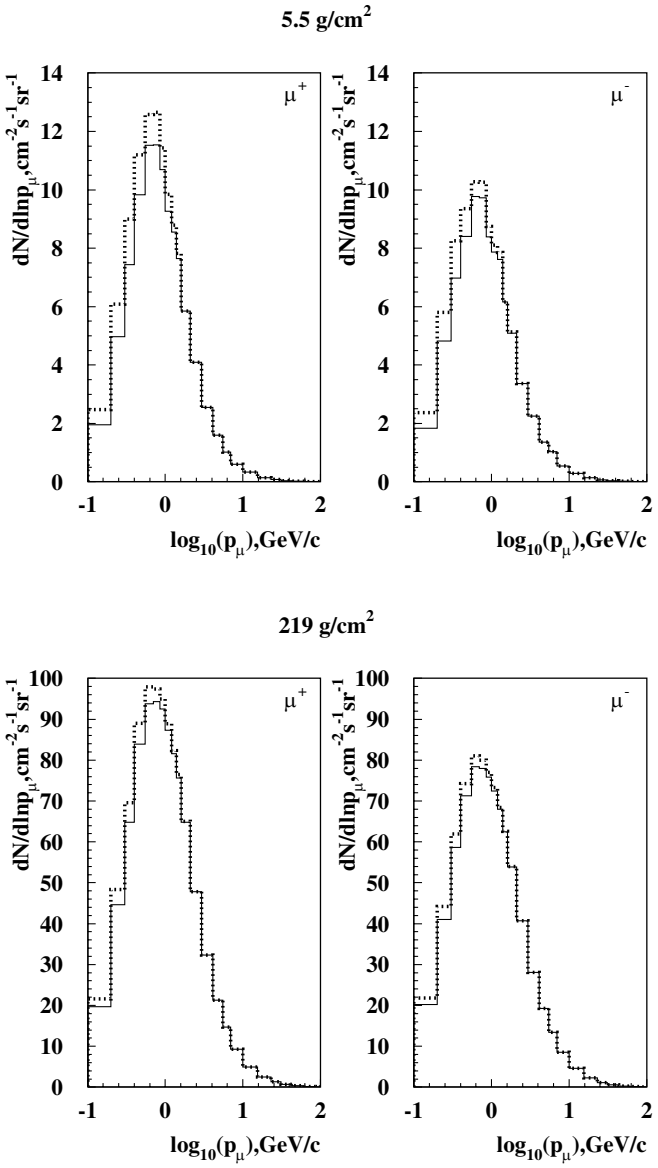

FIG. 5. Simulated muon fluxes at Fort Summer for atmospheric depths of 5.5 and 219 g/cm^2 applying the theoretical geomagnetic transmission function that select only primary cosmic rays from the West (dotted histogram); and from the East (solid histogram).

B. Geomagnetic field effects

The magnetic field affects the low-energy muon flux both through the geomagnetic cutoffs on the primary cosmic rays, including the East-West effect, and by the bending of trajectories of secondary charged particles inside the atmosphere.

The East-West effect is the suppression of cosmic ray nuclei incident on the atmosphere from the East compared to those from the West. This suppression is due to the combination of the following two facts [20,21]:

(i) Positively charged particles at the same zenith angle have a higher cutoff from the East direction than from the West (and vice-versa for negatively

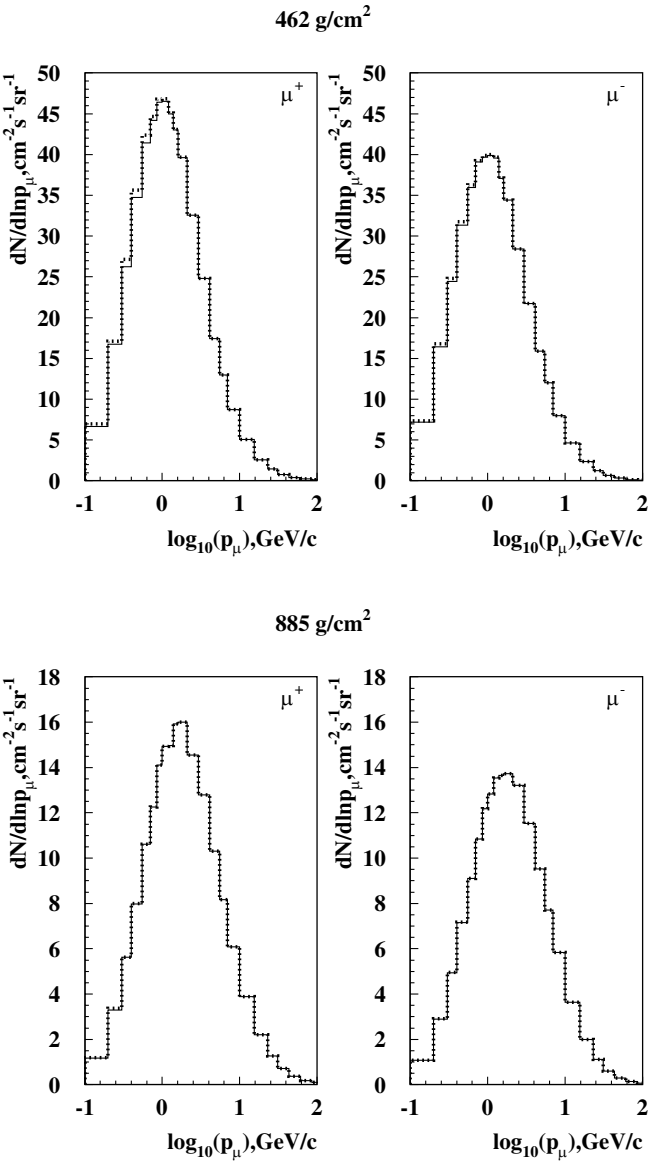

FIG. 6. Same as Fig. 5 for 462 and 885 g/cm^2

charged particles) since some of their trajectories intersect the Earth.

(ii) Cosmic rays are positively charged nuclei, so they will bend systematically in one sense in the geomagnetic field.

To calculate these geomagnetic effects we use backtracking technique in a detailed, time-dependent geomagnetic field model (IGRF, International Geomagnetic Field model) tuned to the period of the experiment. This technique consists of the integration of the equation of motion of a particle with the opposite charge starting at a position near the top of the atmosphere. We inject antiprotons outwards from an altitude of 100 km in various directions and see if the backtracked antiproton reaches a distance of 30 $R_\oplus$ from the Earth within a total path-length of 300 $R_\oplus$. Comparisons [22] with Stoermer's analytical calculation in a dipole magnetic field model show an accuracy of about 1%. Any direction in which an antiproton of a given momentum can reach this distance is an allowed direction from which a proton of the opposite momentum can arrive. The backtracked antiprotons that do not reach that distance are either trapped in the geomagnetic field or their trajectories intersect the surface of the Earth. In these last two cases the trajectory is considered forbidden. The penetration of a charged particle into the atmosphere is either forbidden or allowed for fixed rigidity, angle and atmospheric depth, i.e. the penetration probability is either 0 or 1. When averaged in rigidity and angle, however, it can be expressed in terms of a transmission function, which is zero at low rigidity and increases to one at higher rigidity. The rigidity dependence of the transmission function varies with the geomagnetic latitude and the angle between the cosmic ray direction and the geomagnetic field lines. The geomagnetic cutoff is treated in the simulation by the application of this function to the input primary cosmic ray flux. To explore the East-West effect we have constructed two transmission functions as a function of the cosmic ray zenith angle, one for primaries coming within 30° from the East and a similar cone from the West.

The CAPRICE Geomagnetic transmission function [23] used in Ref. [15] was obtained by comparing the shape of

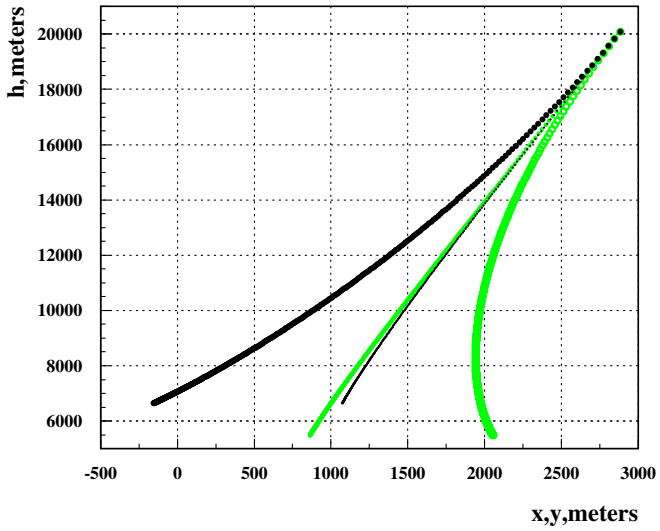

FIG. 7 (color online). A positive and a negative 1 GeV/c muon injected at 20 Km with $\cos(\theta) = 0.98$ and azimuth $= 45^0$ bending in the Geomagnetic field at Fort Sumner in x and y direction and followed until decay. *(1)* Narrow light line: Negative muon deflection in *x* direction. *(2)* Wide light line: Negative muon deflection in *y* direction. *(3)* Narrow solid line: Positive muon deflection in *x* direction. *(4)* Wide solid line: Positive muon deflection in *y* direction. The particle bending depend on the azimuth angle and is stronger when the particles are perpendicular to *B*.

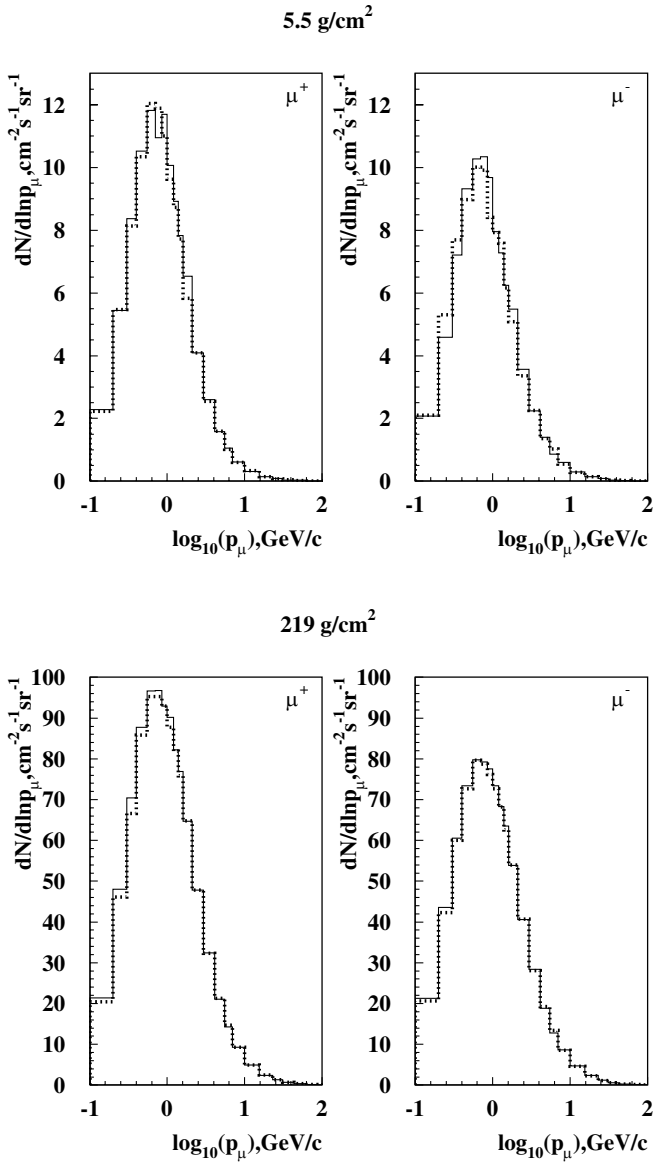

FIG. 8. Comparison of field off (solid) with field on (dotted) for cascade development. Muon fluxes are shown for 5.5 and 219 g/cm^2. Difference arise from bending of muones in the local geomagnetic field.

the spectra of alpha particles measured by the balloon borne experiment CAPRICE94 [24] with the shape of CAPRICE98 [25]. These two balloon experiments flew in different locations: the first in Lynn Lake, Manitoba, Canada, where the geomagnetic cutoff (0.58 GV) is below the pion production threshold for protons, and the other in Ft. Summer New Mexico (USA) where the vertical cutoff is 4.3 GV. This transmission function is only a function of rigidity and therefore does not produce the East-West effect. We compare the two methods in Sec. III below.

C. The low and high fits to the primary spectrum data

New measurements of the primary spectra of protons and helium have improved our knowledge of the primary spectrum up to 100 GeV compared to what was previously known. There are nevertheless still significant discrepancies between different experiments. For this reason we have performed two different fits: one with the experiments that give the lowest (we will call them Group 1) and another that give the highest fluxes (Group 2). All these measurements were fitted to the following function:

$$\phi(E_k) = k(E_k + b\ \exp(-c\sqrt{E_k}))^{-\alpha} \qquad (1)$$

where E_k is the kinetic energy per nucleon [26], and α and k are free parameters.

Group 1 consists of the data of CAPRICE98 [23] below 100 GeV and Atic [27,28] RunJob [30,31] at high energy. Group 2 consists of the data of AMS [31,32], BESS [33] at low energy and JACEE [34] at high energy. In Fig. 1 we

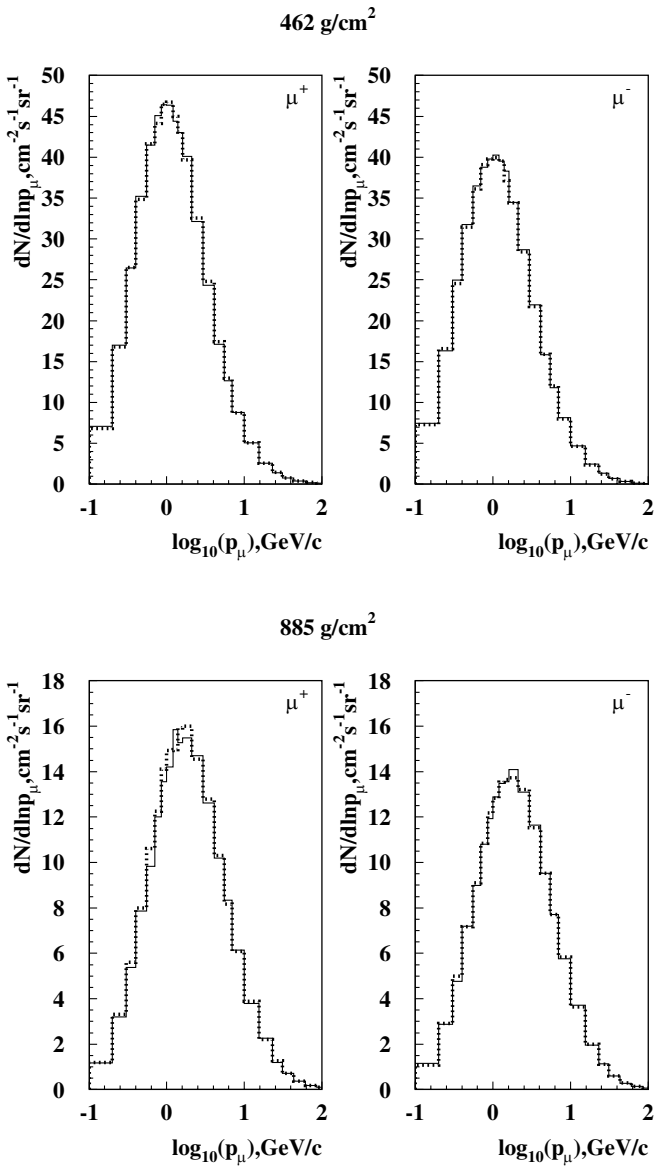

FIG. 9. Same as Fig. 8 for 462 and 885 g/cm^2.

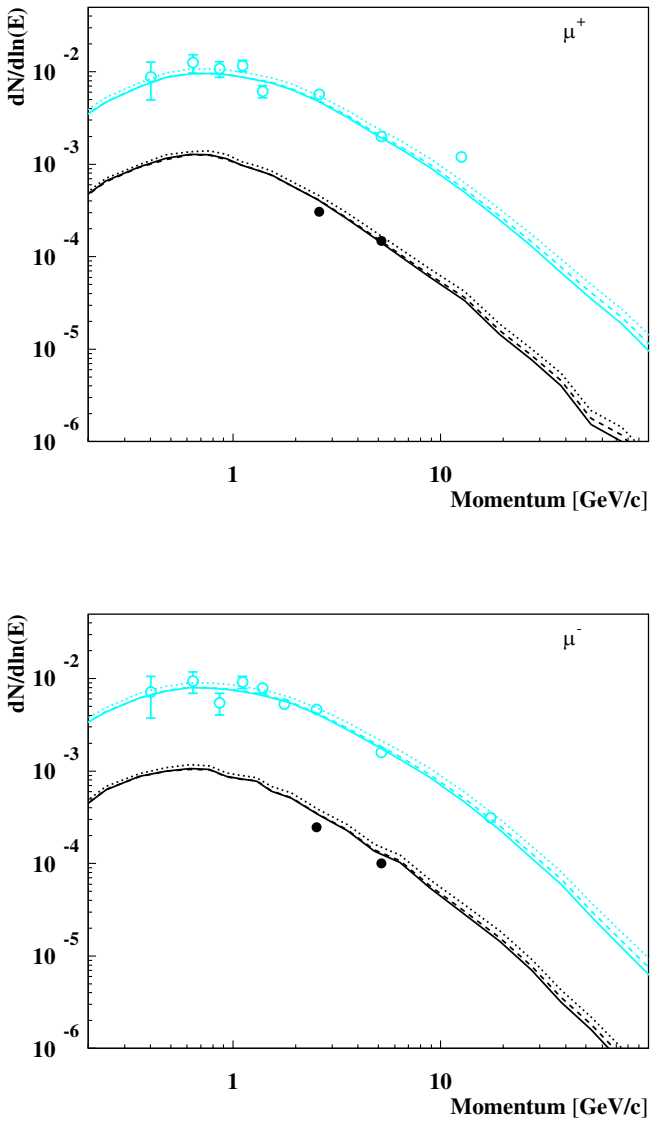

FIG. 10 (color online). μ^+ and μ^- fluxes at 5.5 g/cm^2 (heavy lines) and at 219 g/cm^2 (light lines). Dashed: Simulated muon flux using as input Group 1. Dotted: Group 2. Solid: Ref. [15]. The full (open) circles correspond to the experimental muon data of CAPRICE98 [36] at 5.5 g/cm^2 (219 g/cm^2) of residual atmospheric depth.

show the combination of the experimental data on the proton fluxes for the experiments of group 1 (upper panel) and for group 2 (lower panel). Three different fits are shown for group 1. The solid line corresponds to the fit of all the data. We have also made separate fits for the low-energy data (the dashed line) and for the high energy data (the dotted line). The lower panel of the Fig. 1 shows the proton data from AMS with full circles, BESS with open circles and JACEE with stars. We have done two fits for the following two groups AMS-JACEE (solid line) and BESS-JACEE (dashed line). There was not a considerable difference between AMS-JACEE ($k = 14778 \pm 209$, $\alpha = 2.737 \pm 0.004$) and BESS-JACEE ($k = 14946 \pm 160$, $\alpha = 2.737 \pm 0.003$) fit for the protons fluxes.

Figure 2 shows the helium experimental data for group 1 (upper panel) and group 2 (lower panel). For group 1 we have made two fits with different values of b and c. For group 2 there is a considerable offset between the data of AMS and JACEE. This is not the case in a combination of BESS and JACEE data. For this reason we implement the BESS-JACEE data fit in the calculation. The parameters for the fluxes of group 1 and group 2 are shown in Table I. To have a clear picture we show in Fig. 3 three different fits of the absolute fluxes of proton (upper panel) and helium (lower panel) that we will use in this calculation (Group 1, Group 2 and that of Ref. [15]).

The fluxes of H and He were complemented by fluxes of heavy nuclei in eight groups that were fitted to the available data as in Ref. [15]. The extensions of the spectra of heavy nuclei are not important for the calculations of the atmospheric muon fluxes because H and He nuclei provide 85 to 90% of the all nucleon fluxes. The potential error from inexact fitting of the spectra of heavy nuclei would not exceed 3% of the all nucleon flux. It is the normalization of the proton fluxes that dominates the difference in muon fluxes between group 1 and group 2.

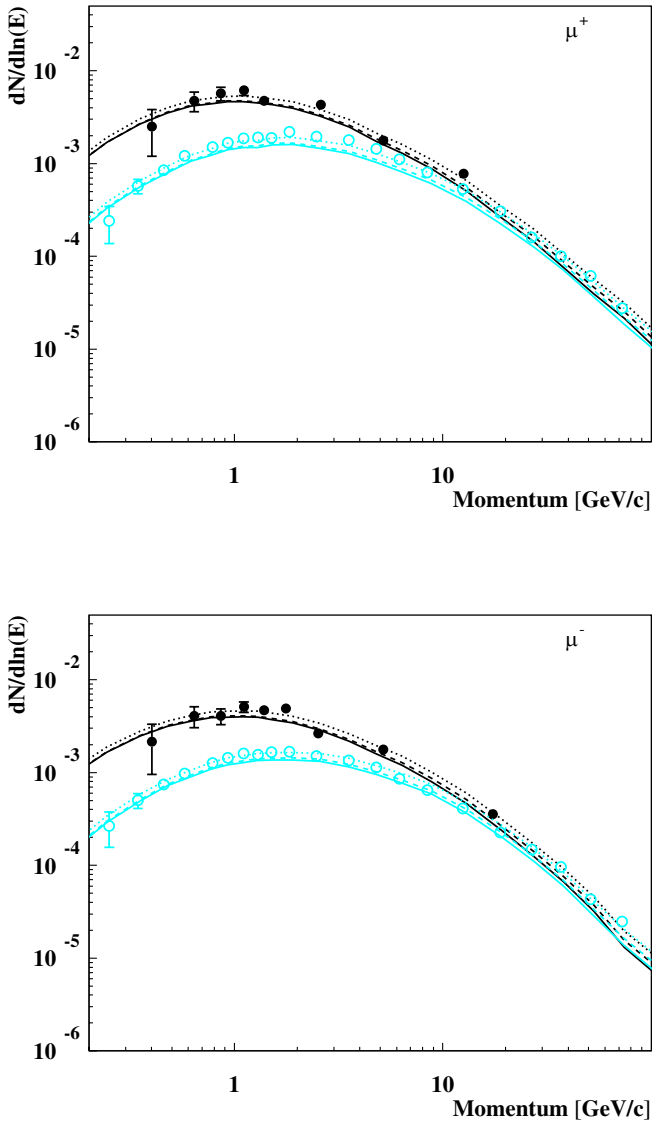

FIG. 11 (color online). Same as Fig. 10 at 462 g/cm^2 (heavy lines and symbols) and at 885 g/cm^2 (light lines and symbols).

III. RESULTS

In the present work, we simulated showers with primary energies from 750 MeV to 10^6 GeV. In order to simulate the absolute fluxes accurately, and also to optimize the statistics, it was convenient to divide the primary energy range into many subintervals with boundaries chosen so that we can approximate the spectrum as a power law within each interval. Independent sets of simulated showers were generated for each of the intervals from an isotropic arrival direction distribution with zenith angles ranging from 0° to 89°.

The shower simulations performed for this study add up to more than 300×10^6 showers, generating particle data files with a total size of about 30 GB, and requiring about 20 days of processing time (using a 1 GHz processor). The Monte Carlo statistic is very large so statistical fluctuation of mean values can be neglected (see [15]).

A. Geomagnetic field effects.

To check the validity of the transmission functions we have calculated the flux of protons at an altitude of 5.5 g/cm^2 where we have experimental results from the CAPRICE98 experiment taken at Ft Summer, New Mexico where the vertical geomagnetic cutoff is 4.3 GV. In Fig. 4 the proton flux at 5.5 g/cm^2 is plotted on the left as a function of momentum. The full points correspond to the data of the proton flux at 5.5 g/cm^2 from CAPRICE98 experiment [35] and the lines are the proton fluxes obtained by the AIRES simulation. The narrow solid line is without applying any transmission function, the wide solid line is using the CAPRICE transmission function and the dotted is applying the theoretical transmission function. We are able to reproduce quite well the proton flux at 5.5 g/cm^2 [35]

using both the CAPRICE and the theoretical transmission functions.

To illustrate the East-West effect we apply to our input flux the theoretical geomagnetic transmission function but selecting primaries particles that only came from the East or from the West. In Fig. 4 on the right the dotted line corresponds to the flux of protons calculated using the theoretical geomagnetic transmission function from the West. The wide solid line corresponds to protons from the East. There is a definite excess of protons that come from the West, which reaches a maximum of about a factor of 2 below 4 GeV.

The effect of this excess on the muon fluxes is illustrated in Figs. 5 and 6. In these two figures we plot the muon flux coming from the West (dotted line) and coming from the East (solid line) as a function of the momentum. In the two figures it is possible to see that the excess of muons coming from the West decreases with increasing atmospheric depth and is negligible at the ground. To quantify the results we calculate the relative differences between the East-West fluxes for positives and negative muons. It was found that the relative differences between the two directions for muons of energy around 0.2 GeV is of order of 25% at 5.5 g/cm^2, 10% at 219 g/cm^2, 5% at 462 g/cm^2 and null at ground.

The muon flux also changes because of the bending in the local magnetic field inside the atmosphere. Figure 7 illustrates this effect by comparing two trajectories, one of

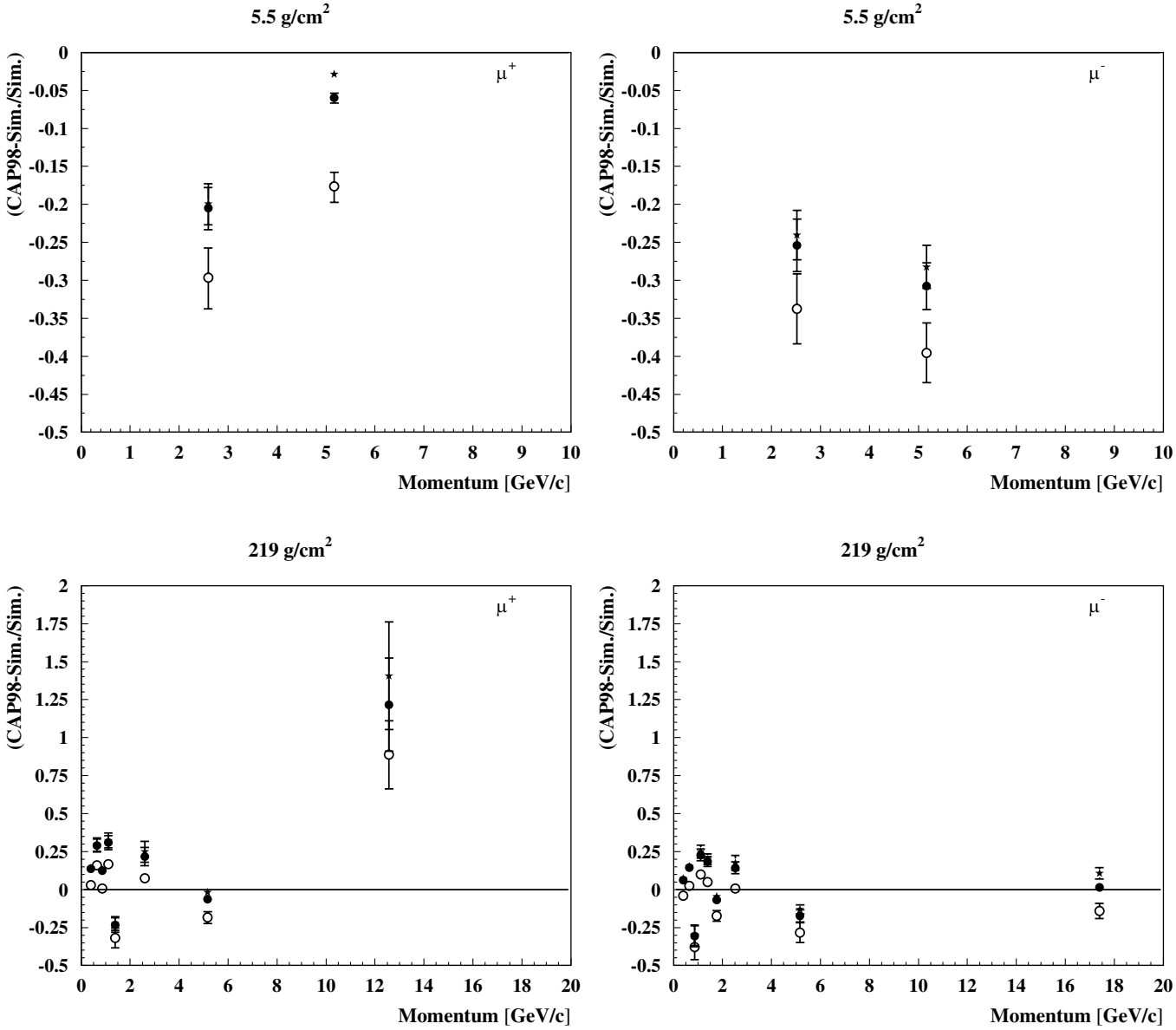

FIG. 12. Relative difference between μ^+ and μ^- fluxes obtained from the CAPRICE98 experiment and the simulations at 5.5 and 219 g/cm^2 Full circle: using as input Group 1. Open circle: using as input Group 2. Star: using as input Ref. [15].

a positive muon, the other of a negative muon. We injected a positive and a negative muon, each of 1 GeV, at 20 Km with zenith angle of 11° and azimuth of 45°. The muons were followed until decay in the geomagnetic field at Fort Sumner. Dark lines show $x-y$ projections of a negative muon; light lines show positive muons. In this illustration the positive muon decays before reaching an altitude of 6000 meters, while the negative muon penetrates past that depth before decaying. In addition, some muons bend away from the Earth, outside the opening angle of the (vertical) muon detector. Such variations in the muon tracks will produce a change in the muon fluxes.

To see the effect of the track bending, we compare two calculations, one with field on and one with field off for the calculation of the atmospheric cascades. Both calculations use the full theoretical treatment of the geomagnetic cutoffs. Fluxes are shown as a function of momentum in Figs. 8 and 9 at several depths in the atmospheres. Small differences persist even to the ground.

B. Muon fluxes from different primary protons and helium spectra.

We study the uncertainty in the predicted muon fluxes by using three different primary spectra of protons and helium in the calculation: group 1, group 2 and those from Ref. [15]. Figs. 10 and 11 show the fluxes of positive and negative muons as a function of momentum using as input Group 1 (dashed line), Group 2 (dotted line) and that of Ref. [15] (solid line). The experimental data are from CAPRICE98.

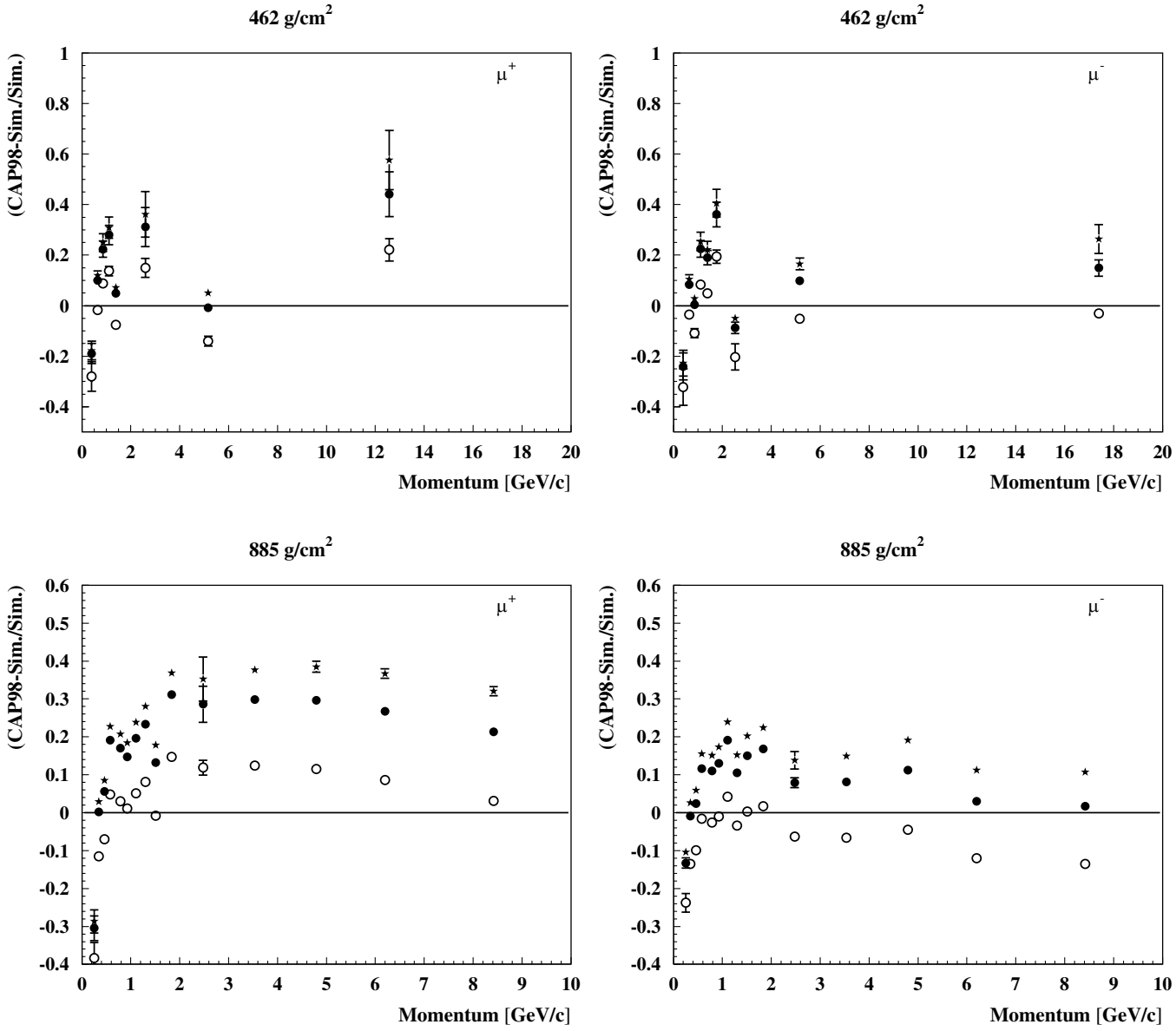

FIG. 13. Same as Fig. 12 for 462 and 885 g/cm^2.

To clarify these differences we show the relative difference between the CAPRICE98 data and the three results of the simulation in Figs. 12 and 13. Here one can see that the higher cosmic ray input fits the experimental data somewhat better. To quantify the results we also calculate the relative differences between μ^+ and μ^- fluxes obtained from group 1 and group 2 ($\frac{\text{Group 2}-\text{Group 1}}{\text{Group 1}}$). At all altitudes the relative difference between the muon fluxes is less than 30% at energies around 180 GeV and less than 20% at energies lower than 20 GeV. The difference in the calculated muon charge ratio μ^+/μ^- with the different inputs is very small, less than 1%. There is a systematic shift in the ratio of calculated to measured fluxes as a function of depth in the atmosphere. At float altitude (5.5 g/cm^2) all calculation are above the data. At ground (885 g/cm^2) the calculations with the lower normalization of the primary spectrum (group 1 and Ref. [15]) are systematic lower than the data, where the higher normalization is in better agreement.

IV. CONCLUSION

We have made an analysis of the effect of the geomagnetic field outside and inside the atmosphere. The differences in the muon fluxes due to the effect of the magnetic field outside the atmosphere decrease with increasing atmospheric depth. The reason is that muons on the ground are generated by higher energy cosmic rays that suffer much less from the geomagnetic cutoff. This is not the case for the effects due to the local magnetic field. This effect is nearly the same at all altitudes. The reason is that muons with higher energy do not easily decay and have longer path-lengths that compensate for the smaller amount of bending per unit path-length.

We also include a calculation of the East-West effect and see the difference in the muon fluxes coming from these directions. These differences increase at low geomagnetic latitude. They are mostly important at float altitude.

After that we also study the effect of different primary cosmic ray spectra on the predicted muon flux. The best agreement with CAPRICE data that we find is for a higher parametrization of the primary cosmic ray flux obtained from the data of BESS and JACEE. Differences are most clear at ground level and are of order 20% at low energy and of order 30% at energies above 100 GeV. In this context it is important to note that the interaction model we use (Extended Hillas splitting Algorithm) for interaction below 200 GeV had somewhat higher pion multiplicity than some other models. This reduces the likelihood of accounting for the ground level data by increasing the pions multiplicity still further in order to lower the normalization of the primary spectrum.

ACKNOWLEDGMENTS

This work is supported in part by U. S. Department of Energy contract DE-FG02 91ER 40626.

[1] K. S. Hirata *et al.*, Phys. Lett. B **205**, 416 (1988); K. S. Hirata *et al.*, Phys. Lett. B **280**, 146 (1992).
[2] Y. Fukuda *et al.*, Phys. Lett. B **335**, 237 (1994).
[3] D. Casper *et al.*, Phys. Rev. Lett. **66**, 2561 (1991); R. Becker-Szendy *et al.*, Phys. Rev. D **46**, 3720 (1992).
[4] K. Daum *et al.*, Z. Phys. C **66**, 417 (1995).
[5] M. Aglietta *et al.*, Europhys. Lett. **8**, 611 (1989).
[6] W. W. M. Allison *et al.*, Phys. Lett. B **391**, 491 (1997); T. Kafka, in *Proceedings of the 5th International Workshop on Topics in Astroparticle and Underground Physics, Gran Sasso, Italy, 1997* (unpublished).
[7] Y. Fukuda *et al.*, Phys. Rev. Lett. **81**, 1562 (1998).
[8] S. J. Sciutto, Proc. 27th ICRC (Hamburg) **1**, 237 (2001).
[9] S. J. Sciutto, www.fisica.unlp.edu.ar/auger/aires.
[10] National Aerospace Administration (NASA), National Oceanic and Atmospheric Administration (NOAA) and US Air Force, US standard atmosphere 1976, NASA technical report NASA-TM-X-74335, NOAA technical report NOAA-S/T-76-1562 (1976).
[11] R. Engel, T. K. Gaisser, and T. Stanev, Proc. 26th ICRC (Utah) **1**, 415 (1999).
[12] N. N. Kalmykov and S. S. Ostapchenko, Yad. Fiz. **56**, 105 (1993); Phys. At. Nucl. **56**, (3) 346 (1993); N. N. Kalmykov, S. S. Ostapchenko, and A. I. Pavlov, Bull. Russ. Acad. Sci. (Physics) **58**, 1966 (1994).
[13] S. J. Sciutto, J. Knapp, and D. Heck, Proc. 27th ICRC (Hamburg) **2**, 526 (2001).
[14] J. Knapp, D. Heck, S. J. Sciutto, M. T. Dova, and M. Risse, Astropart. Phys. **19**, 77 (2003).
[15] P. Hansen, *et al.* Phys. Rev. D **68**, 103001 (2003).
[16] S. Roesler, R. Engel, and J. Ranft, hep-ph/0012252.
[17] A. Fasso, J. Ferrari, J. Ranft, and P. R. Sala, in *Proceedings of the Conference on Advanced Montecarlo Physics Particle Transport Simulations and Applications (MC 2000), Lisbon, Portugal, 2000* (unpublished).
[18] R. Engel, *et al.* Proc. 27th ICRC, Hamburg **4**, 1381 (2001).
[19] A. N. Cillis and S. J. Sciutto, J. Phys. G **26**, 309 (2000).
[20] T. H. Johnson, Phys. Rev. **43**, 834 (1933); T. H. Johnson and E. C. Street, Phys. Rev. **44**, 125 (1933).
[21] L. W.Alvarez and A. H.Compton, Phys. Rev. **43**, 835 (1933).
[22] P. Lipari and Todor Stanev, Proc. ICRC (Rome) **1**, 516 (1995).
[23] M. Boezio, *et al.* Astropart. Phys. **19**, 583 (2003).
[24] M. Boezio *et al.*, Phys. Rev. Lett. **82**, 4757 (1999); Phys. Rev. D **62**, 032007 (2000).

[25] M. Ambriola *et al.* Nucl. Phys. B (Proc. Suppl.) **78**, 32 (1999).
[26] T. K. Gaisser *et al.*, Proc. 27th ICRC (Hamburg) **5**, 1643 (2001).
[27] J. P. Wefel *et al.*, Proc. 28th ICRC, Tsukuba, Japan **4**, 1849 (2003).
[28] ATIC Collaboration, H. Ahn, talk at the COSPAR 2004 meeting, Paris (unpublished).
[29] A. V. Apanasenko *et al.* Astropart. Phys. **16**, 13 (2001); T. Shibata (private communication).
[30] RUNJOB Collaboration, A. V. Apanasenko *et al.*, Proc. of the 27th ICRC, Hamburg **5**, 1626 (2001).
[31] J. Alcaraz *et al.* Phys. Lett. B **490**, 27 (2000).
[32] J. Alcaraz *et al.* Phys. Lett. B **494**, 193 (2000).
[33] T. Sanuki *et al.* Astrophys. J. **545**, 1135 (2000).
[34] K. Asakimori *et al.* Astrophys. J. **502**, 278 (1998).
[35] E. Mocchiutti, PhD thesis, Royal Institute of Technology, Stockholm, 2003, available at http://www.particle.kth.se/.
[36] M. Boezio *et al.*, Phys. Rev. D **67**, 072003 (2003).